Powell–Sabin B-splines for smeared and discrete approaches to fracture in quasi-brittle materials

Stefan May[a], René de Borst[b,*], Julien Vignollet[a]

[a] *University of Glasgow, School of Engineering, Rankine Building, Oakfield Avenue, Glasgow G12 8LT, UK*
[b] *University of Sheffield, Department of Civil and Structural Engineering, Sir Frederick Mappin Building, Mappin Street, Sheffield S1 3JD, UK*

Highlights

- A Powell–Sabin B-splines formulation for higher-order gradient damage models.
- A discrete crack model exploiting Powell–Sabin B-splines based on the cohesive-zone concept.
- A remeshing strategy for Powell–Sabin B-splines with discrete cracks.

Abstract

Non-Uniform Rational B-splines (NURBS) and T-splines can have some drawbacks when modelling damage and fracture. The use of Powell–Sabin B-splines, which are based on triangles, can by-pass these drawbacks. Herein, smeared as well as discrete approaches to fracture in quasi-brittle materials using Powell–Sabin B-splines are considered.

For the smeared formulation, an implicit fourth-order gradient damage model is adopted. Since quadratic Powell–Sabin B-splines employ $\mathcal{C}^1$-continuous basis functions throughout the domain, they are well-suited for solving the fourth order partial differential equation that emerges in this higher order damage model. Moreover, they can be generated from an arbitrary triangulation without user intervention. Since Powell–Sabin B-splines are generated from a classical triangulation, they are not necessarily boundary-fitting and in that case they are not isogeometric in the strict sense.

For discrete fracture approaches, the degree of continuity of T-splines is reduced to $\mathcal{C}^0$ at the crack tip. Hence, stresses need to be evaluated and weighted at the integration points in the vicinity of the crack tip in order to decide when the critical stress is reached. In practice, stress fields are highly irregular around crack tips. Furthermore, aligning a T-spline mesh with the new crack segment can be difficult. Powell–Sabin B-splines also remedy these drawbacks as they are $\mathcal{C}^1$-continuous at the crack tip and stresses can be directly computed, which vastly increases the accuracy and simplifies the implementation. Moreover, re-meshing is more straightforward using Powell–Sabin B-splines. A current limitation is that, in three dimensions, there is no procedure (yet) for constructing Powell–Sabin B-splines on arbitrary tetrahedral meshes.

---

* Corresponding author.
 E-mail address: r.deborst@sheffield.ac.uk (R. de Borst).

1. Introduction

Discrete crack models capture crack initiation and propagation by introducing a geometric discontinuity in the domain. In order to model features like crack propagation in arbitrary directions and crack branching in finite element methods, re-meshing must be adopted in order to align the discretisation to the crack path [1,2]. An interesting alternative is the eXtended Finite Element Method (XFEM), which also allows for arbitrary crack propagation, but positions extra degrees of freedom at existing nodes, thus preserving the original topology of the discretisation, see e.g. [3,4] who used linear elastic fracture mechanics, [5–7] who used cohesive zone models, or [8,9] for the extension to crack propagation in fluid-saturated media.

More recently, Non-Uniform Rational B-splines (NURBS) and T-splines have been used for the modelling of crack initiation and propagation using the cohesive-zone approach [10]. The idea of utilising spline functions, which are commonly used in Computer Aided Design (CAD) packages, also for analysis purposes was introduced in [11,12], and is now commonly known as IsoGeometric Analysis (IGA). While in the original paper by Verhoosel et al. [10] a number of interesting examples are shown of the power of the approach, structured T-splines may not be the optimal spline technology for modelling fracture in a discrete sense. This is because the initial mesh needs to be aligned *a priori* with the final crack path [10], which is normally not known beforehand. A further drawback is that the blending functions of T-spline meshes are only $\mathcal{C}^0$-continuous at the crack tip. Thus, stresses have to be computed at integration points in the vicinity of the crack tip, which detracts from one of the advantages of using splines as basis functions compared to standard Lagrangian basis functions, namely that the accuracy of the stress computation is vastly superior. As a final point, it is noted that triangles are usually favoured for discrete fracture models since they are more flexible for re-meshing, while T-splines have a layout which is based on a quadrilateral structure. For these reasons a spline technology which is based on a triangulation, like Powell–Sabin B-splines [13,14], is potentially more attractive for modelling discrete fracture. As an added benefit Powell–Sabin B-splines allow for a direct computation of the stress tensor at the crack tip since they are $\mathcal{C}^1$-continuous in the entire domain. It is noted though, that at present the extension to three dimensions is not trivial.

The difficulties that adhere to discrete crack approaches, in particular in three-dimensional applications, have motivated the development of smeared crack models. They approximate the crack by introducing a damage-like variable and can be extended to three dimensions in a straightforward manner [15]. In non-local and gradient damage models [16–18] the ill-posedness of the boundary value problem that arises at a generic stage of the loading process when exploiting damage models or softening plasticity models, is removed by introducing a non-local quantity, e.g. a non-local equivalent strain. A computationally efficient setting is obtained by treating this non-local quantity as an independent variable, thus leading to a mixed problem.

However, the introduction of non-locality carries some drawbacks. First, boundary conditions are required for the non-local equivalent strain. Furthermore, one or more internal length scale parameters are introduced. Finally, most higher order gradient models require basis functions of a continuity that is higher than $\mathcal{C}^0$. To meet the latter requirement, NURBS and T-splines have been used in [19]. It is noted, however, that their use may be less straightforward for more complicated geometries. Indeed, it is not always easy to preserve the higher continuity throughout the domain, for example when three or more than four NURBS-patches meet at an extraordinary point. In such cases, the use of Powell–Sabin B-splines can be more convenient since they provide basis functions that are $\mathcal{C}^1$-continuous throughout, and can be created from arbitrary triangulations.

This paper starts with a concise introduction to Powell–Sabin B-splines. Next, gradient damage models are considered. Subsequently, Powell–Sabin B-splines are applied to discrete fracture using a cohesive zone model. Index notation has been used with respect to a Cartesian frame throughout the paper.

2. Quadratic Powell–Sabin B-splines

In this section, we give a short introduction to Powell–Sabin B-splines. A more elaborate introduction into Powell–Sabin B-splines is given in [20]. For computational efficiency, Bézier extraction is used for Powell–Sabin B-splines [21].
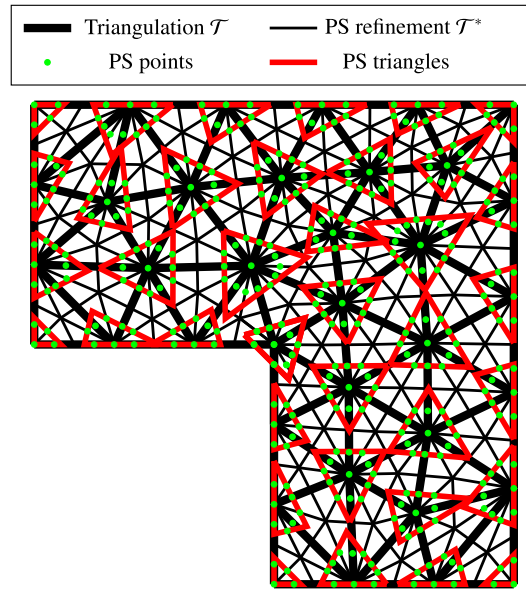
Fig. 1. Triangulation $\mathcal{T}$ (thick black lines), Powell–Sabin refinement $\mathcal{T}^*$ (thin black lines), Powell–Sabin points (green) and Powell–Sabin triangles (red) for an L-shaped geometry. (For interpretation of the references to colour in this figure legend, the reader is referred to the web version of this article.)

2.1. Powell–Sabin B-splines

In order to obtain basis functions with $\mathcal{C}^1$-continuity for a triangulation $\mathcal{T}$, some pre-processing steps are necessary. Each triangle e of the triangulation $\mathcal{T}$ has to be split into six ($n = 1 \ldots 6$) mini-triangles (cf Fig. 1). This yields the Powell–Sabin refinement $\mathcal{T}^*$. Powell–Sabin points (green) are now defined for each vertex k of the triangulation $\mathcal{T}$: they are the vertex k itself and points that lie in the centre of edges of $\mathcal{T}^*$ that contain the vertex k. A Powell–Sabin triangle (shown in red), which contains all Powell–Sabin points, is associated with each vertex k. The Powell–Sabin triangle needs to contain all Powell–Sabin points in order to get positive basis functions. Furthermore, the triangle needs to be small for a low condition number of the stiffness matrix. The Powell–Sabin triangles are chosen in such a way that they share two edges with the convex hull of the Powell–Sabin points [22,23]. In this manner the solution of an expensive optimisation algorithm is avoided [20]. We further constrain the Powell–Sabin triangles on the boundary as follows: for an angle of $\gamma < 180°$ two edges of the Powell–Sabin triangle lie on the boundary; for an angle of $\gamma = 180°$, one edge of the Powell–Sabin triangle lies on the boundary, Fig. 1. No restriction is imposed on Powell–Sabin triangles at an internal discontinuity (see also Section 4).

After computing a Powell–Sabin triangle for each vertex k, the basis functions can be computed. Three ($j = 1, 2, 3$) Powell–Sabin B-splines N_k^j are associated with each vertex k, with coordinates $\underline{V}_k = (x_k, y_k)$ of the triangulation $\mathcal{T}$ and have the following properties. For any $l \neq k$ we have

$$N_k^j(V_l) = 0, \qquad \frac{\partial}{\partial x} N_k^j(V_l) = 0, \qquad \frac{\partial}{\partial y} N_k^j(V_l) = 0, \tag{1}$$

and otherwise

$$N_k^j(V_k) = \alpha_k^j, \qquad \frac{\partial}{\partial x} N_k^j(V_k) = \beta_k^j, \qquad \frac{\partial}{\partial y} N_k^j(V_k) = \gamma_k^j, \tag{2}$$

with

$$\sum_{j=1}^3 \alpha_k^j = 1, \qquad \sum_{j=1}^3 \beta_k^j = 0, \qquad \sum_{j=1}^3 \gamma_k^j = 0. \tag{3}$$
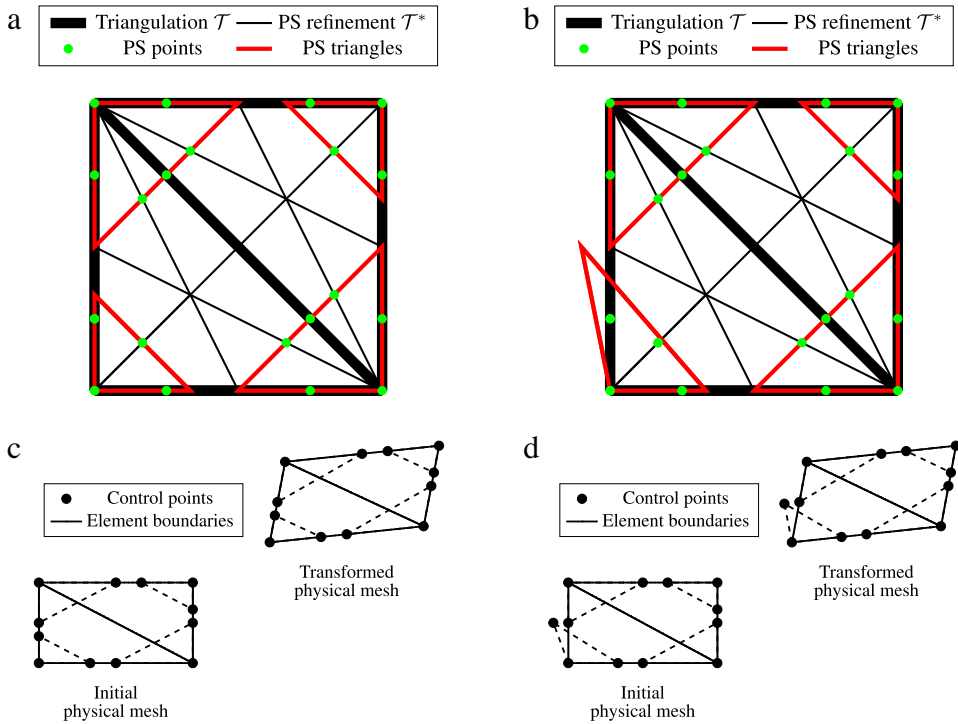
Fig. 2. A triangulation $\mathcal{T}$ consisting of two elements with a different choice for the bottom left Powell–Sabin triangle in (a) and (b). Both options yield an affine transformation in (c) and (d) since the Powell–Sabin B-splines form a partition of unity.

The coefficients α_k^j, β_k^j and γ_k^j in Eq. (3) can be obtained for each vertex k by solving

$$
\begin{bmatrix} \alpha_k^1 & \alpha_k^2 & \alpha_k^3 \\ \beta_k^1 & \beta_k^2 & \beta_k^3 \\ \gamma_k^1 & \gamma_k^2 & \gamma_k^3 \end{bmatrix} \begin{bmatrix} x_k^1 & y_k^1 & 1 \\ x_k^2 & y_k^2 & 1 \\ x_k^3 & y_k^3 & 1 \end{bmatrix} = \begin{bmatrix} x_k & y_k & 1 \\ 1 & 0 & 0 \\ 0 & 1 & 0 \end{bmatrix},
\tag{4}
$$

where $\underline{Q}_k^j = (x_k^j, y_k^j)$ are the coordinates of the Powell–Sabin triangle corners that correspond to vertex k. Once the coefficients α_k^j, β_k^j and γ_k^j have been determined, the Bézier ordinates can be computed in each mini-triangle n of element e for the basis functions $\underline{N}_n^e$. The Bézier ordinates are assembled in the Bézier extraction operator $\underline{\underline{C}}_n^e$. This allows for an efficient computation of the basis functions and their derivatives. For instance, the basis functions $\underline{N}_n^e$ are computed from

$$
\underline{N}_n^e = \underline{\underline{C}}_n^e \underline{B},
\tag{5}
$$

where $\underline{B}$ is the vector containing the Bernstein polynomials. Further details on the calculation of the basis functions $\underline{N}_n^e$ using Bézier extraction can be found in [21].

2.2. Patch test

Special care must be taken for the selection of the Powell–Sabin triangles in order to pass the patch test. For instance, consider the triangulation $\mathcal{T}$ in Figs. 2(a) and (b) consisting of two elements. Figs. 2(a) and (b) show two different options for the bottom left Powell–Sabin triangle. The bottom left Powell–Sabin triangle in Fig. 2(b) is valid since it contains all Powell–Sabin points that correspond to the bottom left vertex. Both options yield an affine transformation when applying to the control points $\underline{P}^i = \underline{Q}^i$ the transformation

$$
\underline{P}_{\mathrm{T}}^i = \underline{\underline{A}} \underline{P}^i + \underline{b}
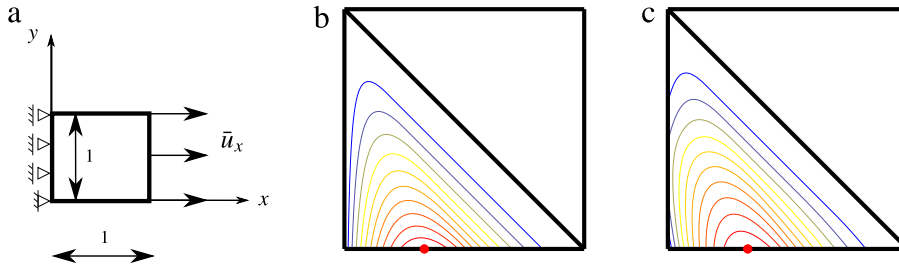\tag{6}
$$

Fig. 3. (a) Patch test for the meshes in Figs. 2(a) and (b). (b) The mesh in Fig. 2(a) passes the patch test — the basis function of the red control point is zero along the left edge. (c) The mesh in Fig. 2(b) with the modified bottom left Powell–Sabin triangle does not pass the patch test—the red control point has a non-zero basis function along the left edge due to the modified Powell–Sabin triangle. (For interpretation of the references to colour in this figure legend, the reader is referred to the web version of this article.)

with the transformation matrix $\underline{\underline{\mathbf{A}}}$, the displacement vector $\underline{\boldsymbol{b}}$ and the control points $\underline{\boldsymbol{P}}_T^i$ after the transformation, as depicted in Figs. 2(c) and (d) since the basis functions fulfil the partition of unity property.

The mesh in Fig. 2(a) also passes the patch test depicted in Fig. 3(a). Fig. 3(b) shows the contour of the basis function for the red control point corresponding to the mesh in Fig. 2(a). The basis function in Fig. 3(b) is zero along the left edge. Shifting the corner of the bottom left Powell–Sabin triangle as in Fig. 2(b) results in a different basis function for the red control point in Fig. 3(c): the basis function is now non-zero along the left edge. Furthermore, the mesh in Fig. 2(b) does not pass the patch test—applying the boundary conditions in Fig. 3(a) does not result in a constant stress in the x-direction.

3. Higher order gradient damage model

In this section, the formulation and numerical elaboration of the implicit higher order gradient damage model is given. Two examples are presented, including the advantages compared to NURBS and T-splines regarding the discretisation.

3.1. Continuum formulation

Higher order gradient damage models require the solution of two coupled field problems. The first field problem to be solved is the equilibrium equation:

$$\sigma_{ij,i} = 0 \tag{7}$$

subject to the boundary conditions

$$\sigma_{ij} n_j = h_i \quad \text{on } \partial \Omega_h, \qquad u_i = \bar{u}_i \quad \text{on } \partial \Omega_u, \tag{8}$$

with the decomposition of the boundary $\partial \Omega$ into the parts $\partial \Omega_h$ and $\partial \Omega_u$ ($\partial \Omega_h \cap \partial \Omega_u = \emptyset$, $\partial \Omega_h \cup \partial \Omega_u = \partial \Omega$), and the prescribed surface traction $\boldsymbol{h}$, the prescribed displacement $\bar{\boldsymbol{u}}$ and the normal vector $\boldsymbol{n}$ on the external boundary. The stress tensor is computed from

$$\sigma_{ij} = (1 - \omega) C_{ijkl} \varepsilon_{kl}, \tag{9}$$

with $\boldsymbol{C}$ the elasticity tensor of the undamaged material, and

$$\varepsilon_{ij} = \frac{1}{2} \left(u_{i,j} + u_{j,i} \right) \tag{10}$$

the infinitesimal strain tensor. $\boldsymbol{u}$ is the displacement vector and $\omega \in [0, 1]$ is the scalar-valued damage parameter ($\omega = 0$ in the undamaged state, $\omega = 1$ in the fully damaged state). The damage parameter ω is a function of a monotonically increasing history parameter κ, $\omega = \omega(\kappa)$. In order to ensure that κ can only grow, the

Karush–Kuhn–Tucker [24,25] conditions

$$f \leq 0, \ \dot{\kappa} \geq 0, \quad \dot{\kappa} f = 0 \tag{11}$$

need to be satisfied. Monotonicity of κ involves monotonicity of ω.

Herein, the loading function $f = \bar{\eta} - \kappa$ is used, with $\bar{\eta}$ the non-local equivalent strain. The latter quantity is defined as the volume average of the local equivalent strain η

$$\bar{\eta}(\underline{x}) = \frac{\int_{\Omega} g(\underline{x}, \underline{\tilde{x}}) \eta(\underline{\tilde{x}}) \mathrm{d}\underline{\tilde{x}}}{\int_{\Omega} g(\underline{x}, \underline{\tilde{x}}) \mathrm{d}\underline{\tilde{x}}} \quad \text{with } g(\underline{x}, \underline{\tilde{x}}) = \exp\left(-\frac{\|\underline{x} - \underline{\tilde{x}}\|}{2l_c^2}\right) \tag{12}$$

the weighting function and l_c the length scale parameter. Expressing the local equivalent strain $\eta(\underline{\tilde{x}})$ in a Taylor series around $\underline{\tilde{x}} = \underline{x}$ and since point $\underline{x}$ takes all values in $\underline{\tilde{x}}$, i.e. $\underline{x}$ and $\underline{\tilde{x}}$ are equivalent, we obtain

$$\bar{\eta}(\underline{x}) = \eta(\underline{x}) + \frac{l_c^2}{2} \eta_{,ii}(\underline{x}) + \frac{l_c^4}{8} \eta_{,iijj}(\underline{x}) + \dots. \tag{13}$$

We differentiate Eq. (13) twice and multiply by $\frac{l_c^2}{2}$, and subsequently differentiate Eq. (13) four times and multiply by $\frac{l_c^2}{8}$. The resulting identities are combined with Eq. (13) to give:

$$\bar{\eta} - \frac{l_c^2}{2}\bar{\eta}_{,ii} + \frac{l_c^4}{8}\bar{\eta}_{,iijj} = \eta + \frac{l_c^8}{64}\eta_{,iijjkkll} + \dots. \tag{14}$$

Neglecting higher order terms in Eq. (14) results in a fourth order partial differential equation for the non-local equivalent strain $\bar{\eta}$

$$\bar{\eta} - \frac{l_c^2}{2}\bar{\eta}_{,ii} + \frac{l_c^4}{8}\bar{\eta}_{,iijj} = \eta, \tag{15}$$

which must be solved in conjunction with Eq. (7). The boundary conditions

$$\bar{\eta}_{,i} n_i = 0, \qquad \bar{\eta}_{,ij} n_i = 0, \qquad \bar{\eta}_{,ijj} n_i = 0 \tag{16}$$

are imposed since it was observed in [19] that ignoring the boundary terms has a minor effect. Multiplying Eq. (7) by a test function δu_j, Eq. (15) by a test function $\delta\bar{\eta}$, integrating over the domain Ω, exploiting integration by parts, Gauss' theorem and the boundary conditions in Eqs. (8) and (16) finally results in:

$$\int_{\Omega} \delta u_{i,j} \sigma_{ij} \, \mathrm{dV} = \int_{\partial \Omega_h} \delta u_i h_i \, \mathrm{dA},$$
$$\int_{\Omega} \delta\bar{\eta}\bar{\eta} + \frac{l_c^2}{2}\delta\bar{\eta}_{,i}\bar{\eta}_{,i} + \frac{l_c^4}{8}\delta\bar{\eta}_{,ij}\bar{\eta}_{,ij} \, \mathrm{dV} = \int_{\Omega} \delta\bar{\eta}\eta \, \mathrm{dV}. \tag{17}$$

3.2. Discretisation

Discretisation of the domain Ω into E elements,

$$\Omega = \bigcup_{e=1}^{E} \Omega^e, \tag{18}$$

and approximation of the displacement u_i, the non-local strain $\bar{\eta}$ and their derivatives,

$$\begin{aligned}
\underline{u}^e &= \underline{\underline{N}}_u \underline{u}, & \delta\underline{u}^e &= \underline{\underline{N}}_u \delta\underline{u}, & \underline{\varepsilon}^e &= \underline{\underline{B}}_u \underline{u}, & \delta\underline{\varepsilon}^e &= \underline{\underline{B}}_u \delta\underline{u}, \\
\bar{\eta}^e &= \underline{N}_{\bar{\eta}}^T \underline{\bar{\eta}}, & \delta\bar{\eta}^e &= \underline{N}_{\bar{\eta}}^T \delta\underline{\bar{\eta}}, & \underline{\bar{\eta}}_{,i}^e &= \underline{\underline{B}}_{\bar{\eta}} \underline{\bar{\eta}}, & \delta\underline{\bar{\eta}}_{,i}^e &= \underline{\underline{B}}_{\bar{\eta}} \delta\underline{\bar{\eta}}, \\
\underline{\bar{\eta}}_{,ij}^e &= \underline{\underline{B}}_{\bar{\eta}\bar{\eta}} \underline{\bar{\eta}}, & \delta\underline{\bar{\eta}}_{,ij}^e &= \underline{\underline{B}}_{\bar{\eta}\bar{\eta}} \delta\underline{\bar{\eta}},
\end{aligned} \tag{19}$$

with

$$
\underline{u}^e = \begin{bmatrix} u_1^e \\ u_2^e \end{bmatrix}, \qquad \delta\underline{u}^e = \begin{bmatrix} \delta u_1^e \\ \delta u_2^e \end{bmatrix}, \qquad \underline{\varepsilon}^e = \begin{bmatrix} \varepsilon_{11}^e \\ \varepsilon_{22}^e \\ 2\varepsilon_{12}^e \end{bmatrix}, \qquad \delta\underline{\varepsilon}^e = \begin{bmatrix} \delta\varepsilon_{11}^e \\ \delta\varepsilon_{22}^e \\ 2\delta\varepsilon_{12}^e \end{bmatrix},
$$

$$
\underline{\bar\eta}_{,i}^e = \begin{bmatrix} \bar\eta_{,1}^e \\ \bar\eta_{,2}^e \end{bmatrix}, \qquad \delta\underline{\bar\eta}_{,i}^e = \begin{bmatrix} \delta\bar\eta_{,1}^e \\ \delta\bar\eta_{,2}^e \end{bmatrix}, \qquad \underline{\bar\eta}_{,ij}^e = \begin{bmatrix} \bar\eta_{,11}^e \\ \bar\eta_{,22}^e \\ \sqrt{2}\bar\eta_{,12}^e \end{bmatrix}, \qquad \delta\underline{\bar\eta}_{,ij}^e = \begin{bmatrix} \delta\bar\eta_{,11}^e \\ \delta\bar\eta_{,22}^e \\ \sqrt{2}\delta\bar\eta_{,12}^e \end{bmatrix},
$$

$$
\underline{\underline{N}}_u = \begin{bmatrix} N_1 & 0 & N_2 & 0 & \dots \\ 0 & N_1 & 0 & N_2 & \dots \end{bmatrix}, \qquad \underline{\underline{B}}_u = \begin{bmatrix} N_{1,1} & 0 & N_{2,1} & 0 & \dots \\ 0 & N_{1,2} & 0 & N_{2,2} & \dots \\ N_{1,2} & N_{1,1} & N_{2,2} & N_{2,1} & \dots \end{bmatrix},
$$

$$
\underline{N}_{\bar\eta}^T = \begin{bmatrix} N_1 & N_2 & \dots \end{bmatrix}, \qquad \underline{\underline{B}}_{\bar\eta} = \begin{bmatrix} N_{1,1} & N_{2,1} & \dots \\ N_{1,2} & N_{2,2} & \dots \end{bmatrix}, \qquad \underline{\underline{B}}_{\bar\eta\bar\eta} = \begin{bmatrix} N_{1,11} & N_{2,11} & \dots \\ N_{1,22} & N_{2,22} & \dots \\ \sqrt{2}N_{1,12} & \sqrt{2}N_{2,12} & \dots \end{bmatrix}
\tag{20}
$$

gives the following matrix–vector equation for Eq. (17):

$$
\delta\underline{u}^T \underbrace{\int_\Omega \underline{\underline{B}}_u^T (1-\omega)\underline{\underline{C}}\,\underline{\underline{B}}_u\,\mathrm{dV}\underline{u}}_{\underline{f}_u^{\mathrm{int}}(\underline{u},\underline{\bar\eta})} - \delta\underline{u}^T \underbrace{\int_{\partial\Omega_h} \underline{\underline{N}}_u^T \underline{h}\,\mathrm{dA}}_{\underline{f}_u^{\mathrm{ext}}} = 0,
$$

$$
\delta\underline{\bar\eta}^T \underbrace{\left(\int_\Omega \underline{N}_{\bar\eta}\underline{N}_{\bar\eta}^T + \frac{l_c^2}{2}\underline{\underline{B}}_{\bar\eta}^T\underline{\underline{B}}_{\bar\eta} + \frac{l_c^4}{8}\underline{\underline{B}}_{\bar\eta\bar\eta}^T\underline{\underline{B}}_{\bar\eta\bar\eta}\,\mathrm{dV}\underline{\bar\eta} - \int_\Omega \underline{N}_{\bar\eta}\eta\,\mathrm{dV} \right)}_{\underline{f}_{\bar\eta}^{\mathrm{int}}(\underline{u},\underline{\bar\eta})} = 0.
\tag{21}
$$

For arbitrary $\delta\underline{u}$, $\delta\underline{\bar\eta}$ and $\underline{h} = \mathbf{0}$ this yields

$$
\underline{H}(\underline{u},\underline{\bar\eta},\lambda) = \begin{bmatrix} \underline{f}_u^{\mathrm{int}}(\underline{u},\underline{\bar\eta}) - \lambda\underline{\hat{f}} \\ \underline{f}_{\bar\eta}^{\mathrm{int}}(\underline{u},\underline{\bar\eta}) \\ \psi(\underline{u},\lambda) \end{bmatrix} = \mathbf{0},
\tag{22}
$$

where $\lambda\underline{\hat{f}}$ assembles the nodal forces, with $\underline{\hat{f}}$ the normalised load vector and λ the loading parameter. ψ is an arc-length function. In the remainder we employ the arc-length function based on the rates of internal $\dot{\mathcal{U}}$ and dissipated energy $\dot{\mathcal{E}}^D$ from [26]. Linearisation of Eq. (22) yields for the $i+1$th iteration in the $n+1$th increment:

$$
\begin{bmatrix} \underline{u} \\ \underline{\bar\eta} \\ \lambda \end{bmatrix}_{i+1}^{n+1} = \begin{bmatrix} \underline{u} \\ \underline{\bar\eta} \\ \lambda \end{bmatrix}_i^{n+1} - \underline{\underline{K}}_T^{-1}\Big|_i^{n+1} \cdot \begin{bmatrix} \underline{f}_u^{\mathrm{int}}(\underline{u},\underline{\bar\eta}) - \lambda\underline{\hat{f}} \\ \underline{f}_{\bar\eta}^{\mathrm{int}}(\underline{u},\underline{\bar\eta}) \\ \psi(\underline{u},\lambda) \end{bmatrix}_i^{n+1},
\tag{23}
$$

with the tangential stiffness matrix

$$
\underline{\underline{K}}_T(\underline{u},\underline{\bar\eta},\lambda) = \begin{bmatrix} \dfrac{\partial\underline{f}_u^{\mathrm{int}}(\underline{u},\underline{\bar\eta})}{\partial\underline{u}} & \dfrac{\partial\underline{f}_u^{\mathrm{int}}(\underline{u},\underline{\bar\eta})}{\partial\underline{\bar\eta}} & -\underline{\hat{f}} \\[3mm] \dfrac{\partial\underline{f}_{\bar\eta}^{\mathrm{int}}(\underline{u},\underline{\bar\eta})}{\partial\underline{u}} & \dfrac{\partial\underline{f}_{\bar\eta}^{\mathrm{int}}(\underline{u},\underline{\bar\eta})}{\partial\underline{\bar\eta}} & \mathbf{0} \\[3mm] \dfrac{\partial\psi(\underline{u},\lambda)}{\partial\underline{u}} & \mathbf{0}^T & \dfrac{\partial\psi(\underline{u},\lambda)}{\partial\lambda} \end{bmatrix}.
\tag{24}
$$

3.3. Examples

In this section, we first study the L-shaped specimen considered before in [19]. Next, a Single-Edge Notched Beam (SENB) is considered subject to an antisymmetric four-point shear loading.
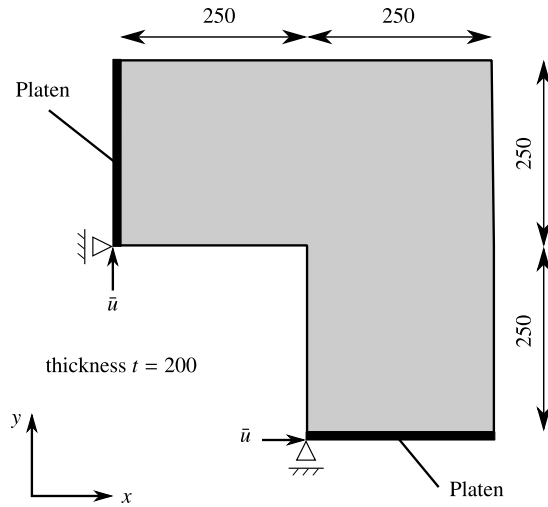
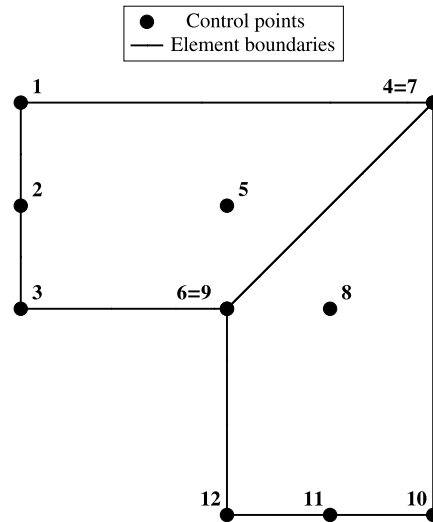Fig. 4. Set-up for the L-shaped specimen (dimensions in mm).

Fig. 5. Quadratic NURBS mesh with $\mathcal{C}^1$-continuity everywhere for the knot vectors $\Xi = \{0, 0, 0, 1, 1, 1\}$ and $\mathcal{H} = \{0, 0, 0, \frac{1}{2}, 1, 1, 1\}$.

3.3.1. L-shaped specimen

The set-up for the L-shaped specimen is given in Fig. 4 and the parameters and coefficients have been chosen according to [19].

The L-shaped specimen has been discretised using NURBS, T-splines and Powell–Sabin B-splines. A $\mathcal{C}^1$-continuous NURBS mesh is depicted in Fig. 5. This mesh contains two pairs of overlapping control points which results in a vanishing determinant of the Jacobian matrix $J_{ij} = \frac{\partial x_i}{\partial \xi_j}$. It has been shown in [27] that these discretisations can still be robust. However, when several NURBS-patches are used, they join with $\mathcal{C}^0$-continuity only. Regaining $\mathcal{C}^1$-continuity, especially when three or more than four NURBS-patches join at an extraordinary point, is cumbersome.

A mesh that is $\mathcal{C}^1$-continuous throughout the L-shaped domain is shown in Fig. 6 for T-splines. According to [28], this T-spline mesh is standard, i.e. all blending functions sum to one. Furthermore, the Bézier extraction operator is a square matrix in each element. It is noted that the blue marked corner in Fig. 6(b) is not interpolatory, i.e. there is no control point. If, instead, the L-shaped specimen is modelled with an interpolatory corner $\mathcal{C}^0$-continuity is introduced. The mesh in Fig. 6 has the disadvantage that it needs to be created by hand.
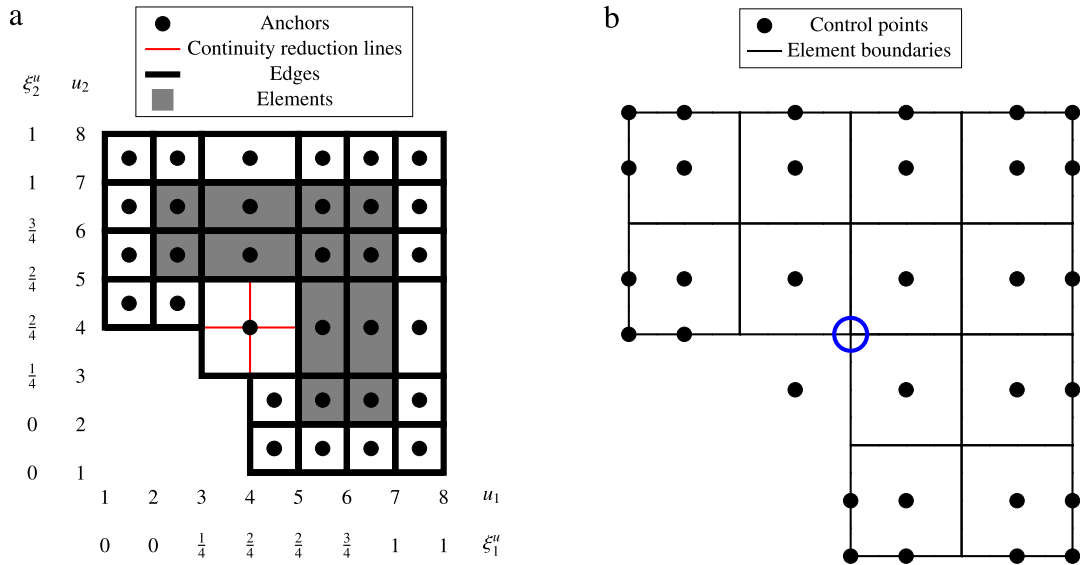
Fig. 6. Quadratic T-spline mesh for the L-shaped geometry with $\mathcal{C}^1$-continuity everywhere in (a) the index (u_ℓ) and parameter (ξ_ℓ^u) domain and (b) the physical (x_ℓ) domain. (For interpretation of the references to colour in this figure legend, the reader is referred to the web version of this article.)
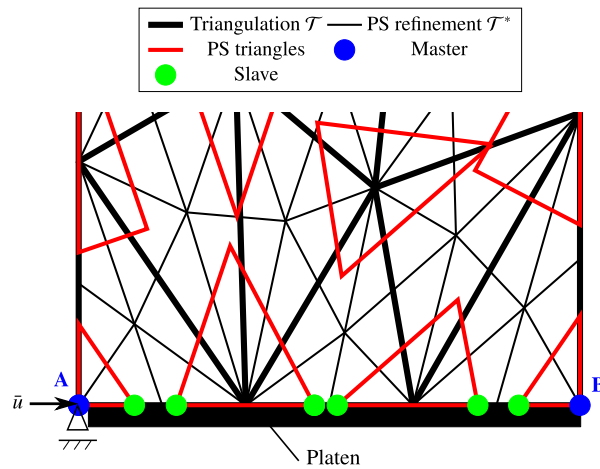

Fig. 7. Linear constraints along the bottom platen in Fig. 4 with Powell–Sabin B-splines.

Alternatively, Fig. 1 shows the Powell–Sabin B-spline mesh that is obtained directly from a standard triangulation. The linear constraints along the platens in Fig. 4 are imposed using a master–slave relation as follows (see also Fig. 7 for the bottom platen). Let $\underline{u}_A$ and $\underline{u}_B$ be the displacement at the left and right corners of the bottom platen with coordinates x_A and x_B, respectively. A and B are the master control points. Then, for any slave control point S with coordinates x_S along the edge, its displacement $\underline{u}_S$ is set to

$$\underline{u}_S = \left(1 - \frac{x_S - x_A}{x_B - x_A}\right)\underline{u}_A + \frac{x_S - x_A}{x_B - x_A}\underline{u}_B. \tag{25}$$

This master–slave relation must be incorporated into Eq. (23) as described in [29]. Note, that Eq. (25) follows from the intercept theorem

$$\frac{\underline{u}_S - \underline{u}_A}{x_S - x_A} = \frac{\underline{u}_B - \underline{u}_A}{x_B - x_A}. \tag{26}$$
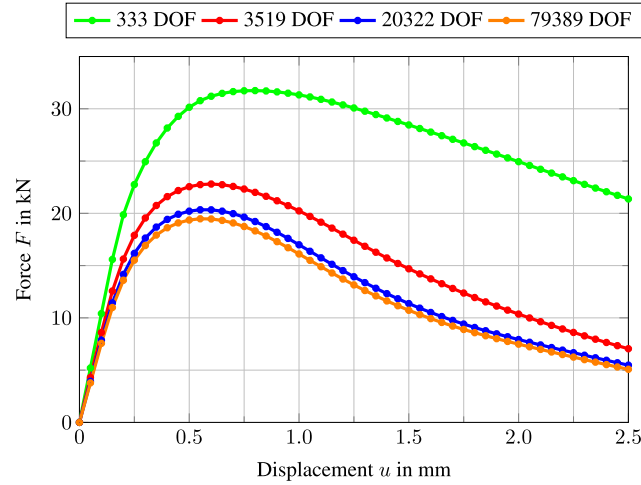
Fig. 8. Force–displacement curves for the L-shaped sample using the implicit fourth-order gradient damage model for four different mesh sizes.

In the calculations, the following parameters have been used: Young's modulus $E = 10,000$ MPa, Poisson's ratio $\nu = 0.2$ and an internal length scale parameter $l_c = 5\sqrt{2}$ mm^2. Plane-stress conditions are assumed. The thickness of the specimen is $t = 200$ mm. The modified von Mises local equivalent strain defined in [30]

$$\eta(\boldsymbol{\varepsilon}) = \frac{k-1}{2k(1-2\nu)} I_1(\boldsymbol{\varepsilon}) + \frac{1}{2k} \sqrt{\left(\frac{k-1}{1-2\nu} I_1(\boldsymbol{\varepsilon})\right)^2 + \frac{12k}{(1+\nu)^2} J_2(\boldsymbol{\varepsilon})}, \tag{27}$$

with the first invariant of the strain tensor,

$$I_1(\boldsymbol{\varepsilon}) = \varepsilon_{kk}, \tag{28}$$

and the second invariant of the deviatoric strain tensor,

$$J_2(\boldsymbol{\varepsilon}) = \frac{1}{2}\varepsilon_{ij}\varepsilon_{ij} - \frac{1}{6}I_1(\boldsymbol{\varepsilon})^2, \tag{29}$$

has been used. In Eq. (27), $k = 10$ is set in order to account for different strengths in compression and tension. The following damage law [31] has been utilised

$$\omega(\kappa) = \begin{cases} 0 & \kappa \leq \kappa_0 \\ 1 - \dfrac{\kappa_0}{\kappa}\Big(1 - \alpha + \alpha \exp\big(\beta(\kappa_0 - \kappa)\big)\Big) & \kappa > \kappa_0 \end{cases}, \tag{30}$$

with the parameters $\kappa_0 = 4 \times 10^{-4}$, $\alpha = 0.98$ and $\beta = 80$.

Displacement control has been applied to the left corner of the bottom platen and the bottom corner of the left platen with an increment of $\Delta\bar{u} = 0.05$ mm. The meshes for the Powell–Sabin B-splines have been refined uniformly.

Fig. 8 shows the force–displacement curves for four different mesh sizes. The legend entry displays the number of degrees of freedom (DOF). Fig. 9 shows the contours for the damage field ω and the first principal stress σ_1 for the mesh with 20,322 degrees of freedom at a displacement $\bar{u} = 1.9$ mm. Finally, Fig. 10 shows a comparison in terms of the force–displacement curve between the second order and the fourth order gradient damage formulations (for the mesh with 20,322 degrees of freedom).

3.3.2. Single-edge notched beam

The second example concerns a Single-Edge Notched Beam (SENB). The parameters and coefficients have been taken from [32]. The geometry and the boundary conditions are depicted in Fig. 11.

The two platens at the top and at the bottom have not been modelled explicitly in the finite element model. Instead, they are incorporated by means of linear constraints with a master–slave dependency as in the previous example. For
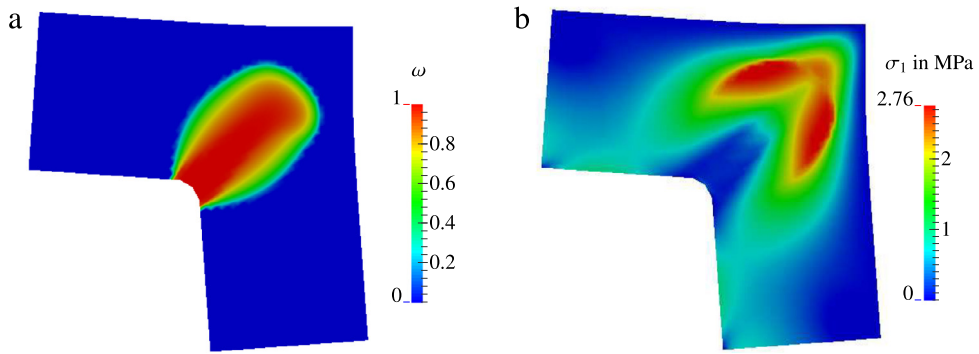
Fig. 9. L-shaped sample in the deformed configuration at a displacement of $\bar{u} = 1.9$ mm for the mesh with 20,322 degrees of freedom. Displacements are amplified by a factor of 20. Contours for (a) damage field ω and (b) first principal stress field σ_1.
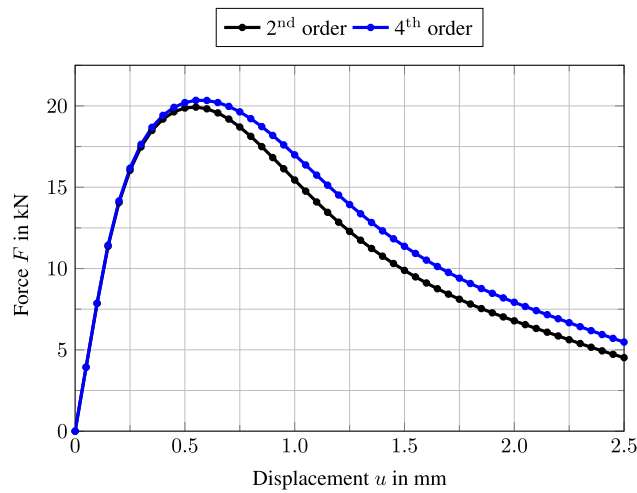

Fig. 10. Force–displacement curves for the L-shaped sample using second and fourth order formulations for the mesh with 20,322 degrees of freedom.
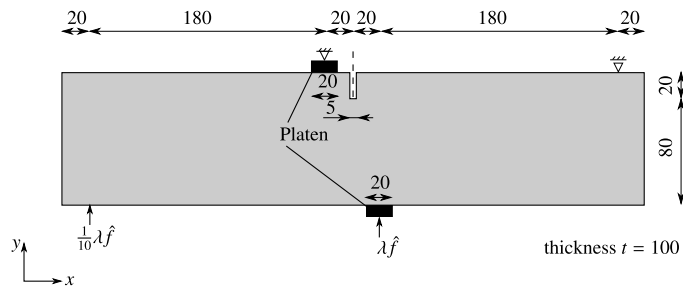

Fig. 11. Set-up for the SENB (dimensions in mm).

the platen at the top (Fig. 12(a)), the displacement of the orange control points (circles) is set to zero. The master control point C is marked blue. The displacement of the slave control points (green) is set to

$$\underline{u}_S = \left(1 - \frac{x_S - x_C}{x_D - x_C}\right)\underline{u}_C. \tag{31}$$

It is noted that at the *vertex* D (which is not a *control point*) the displacement is zero.
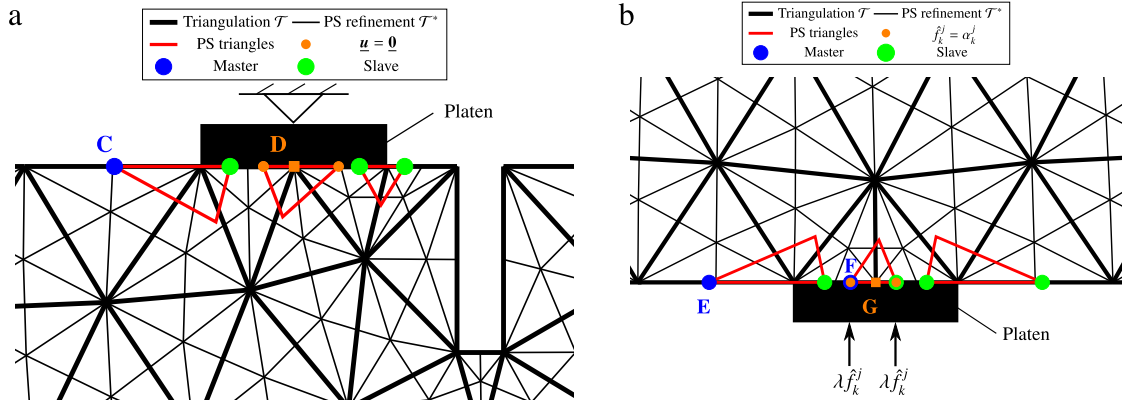
Fig. 12. Applying the linear constraints along the platens in Fig. 11 to the control points. Control points are indicated by circles, vertices by squares. (For interpretation of the references to colour in this figure legend, the reader is referred to the web version of this article.)
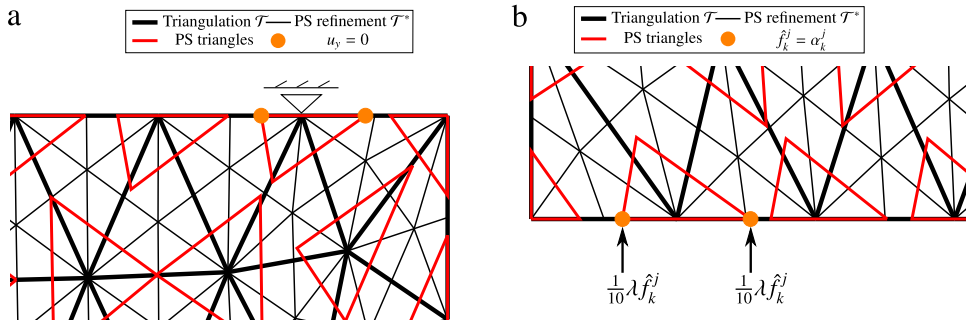

Fig. 13. Applying the boundary conditions in Fig. 11 to the control points.

At the bottom platen (cf. Fig. 12(b)), $\hat{f}_k^j = \alpha_k^j$ has been imposed for the two orange control points (circles). The orange control points correspond to the vertex G marked with an orange square. Since one edge of the Powell–Sabin triangle for vertex G lies on the boundary, we have $\alpha_k^j = 0$ for the third control point. With Eq. (3)a, we get the required prescribed load for the bottom platen. Furthermore, the relation

$$\underline{u}_S = \left(1 - \frac{x_S - x_E}{x_F - x_E}\right) \underline{u}_E + \frac{x_S - x_E}{x_F - x_E}\underline{u}_F \tag{32}$$

has been incorporated into Eq. (23), where S are the slave control points (green) and E and F are the master control points (blue). For the fixed boundary condition at the top right, the displacement in the vertical direction of the two control points (marked orange) in Fig. 13(a) is set to zero. The boundary condition at the bottom left is imposed by setting $\hat{f}_k^j = \alpha_k^j$ for the two control points (orange) in Fig. 13(b).

The material parameters of the concrete are: Young's modulus $E = 35{,}000$ MPa, Poisson's ratio $\nu = 0.2$ with a plane-stress assumption. The thickness of the specimen is $t = 100$ mm. The internal length scale is set to $l_c = \sqrt{2}$ mm^2. The modified von Mises local equivalent strain, Eq. (27), and the damage law Eq. (30) have been used again, but now with $k = 10$, $\kappa_0 = 6 \times 10^{-5}$, $\alpha = 0.96$ and $\beta = 100$. In order to trace the equilibrium path, the arc-length method proposed in [26] has been employed with $\Delta\tau = 8$ kN and $a = 0.25$. The meshes have been refined uniformly.

Fig. 14 shows the force–displacement curves. Along the x-axis the crack mouth sliding displacement (CMSD, the difference in the vertical displacement between the right and the left notch tips) has been plotted, and along the y-axis the force $P = \frac{11}{10}\lambda$.
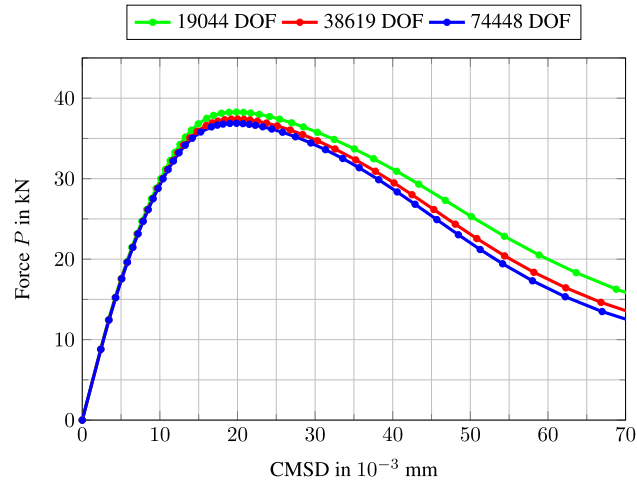
Fig. 14. Force–displacement curves for the SENB with the implicit fourth-order gradient damage model for three different mesh sizes.
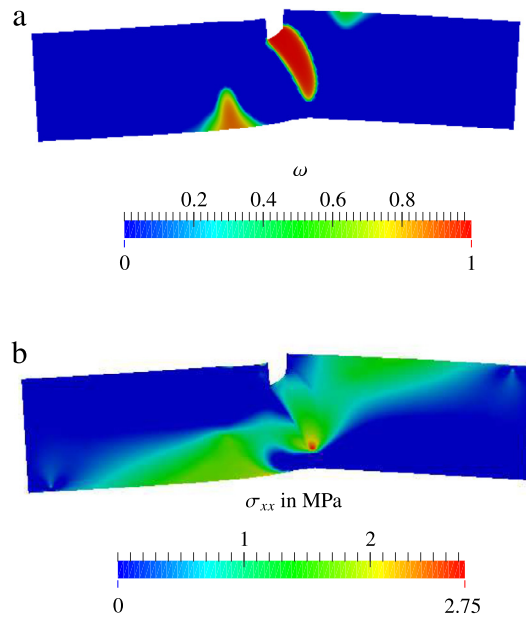

Fig. 15. Single-Edge Notched Beam in the deformed configuration at a CMSD $= 0.04$ mm for the mesh with 74,448 degrees of freedom. Displacements are amplified by a factor of 200. Contours for (a) damage field ω and (b) stress field σ_{xx}.

Fig. 15(a) shows for the Single-Edge Notched Beam with 74,448 degrees of freedom at a CMSD $= 0.04$ mm the damage and stress field ω and σ_{xx}, respectively. It is noted that for coarser meshes (less than 19,044 degrees of freedom), the Single-Edge Notched Beam may fail due to the damage zone which starts to grow at the bottom left edge while the damage zone at the notch does not propagate. Hence, fine meshes are required in order to obtain results that are in agreement with the experiments in [33].

4. Discrete crack modelling

This section introduces a discrete approach to fracture where a cohesive zone model is used for the tractions between the faces of the crack. The re-meshing procedure is explained, and as an example the Single-Edge Notched Beam is considered again.
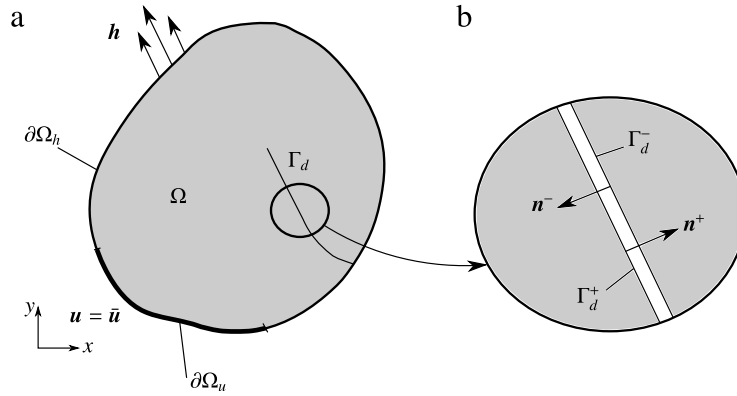
Fig. 16. (a) Domain Ω with internal discontinuity Γ_d and decomposition of the boundary $\partial\Omega$ into $\partial\Omega_h$ and $\partial\Omega_u$. (b) Discontinuity Γ_d with overlapping positive and negative side Γ_d^+ and Γ_D^-, respectively.

4.1. Continuum formulation

For the cohesive zone modelling, a discontinuity Γ_d is present within the domain Ω. It consists of two overlapping boundaries, Γ_d^+ and Γ_d^- see Fig. 16(b). Along each boundary Γ_d^+ and Γ_d^- we impose

$$\sigma_{ij}n_j^+ = t_i^+ \quad \text{on } \Gamma_d^+, \qquad \sigma_{ij}n_j^- = t_i^- \quad \text{on } \Gamma_d^-. \tag{33}$$

t^+ and t^- are the tractions in the cohesive zone on the positive and negative side, respectively. n^+ and n^- are the normal vectors on Γ_d^+ and Γ_d^-. Setting

$$t_i = t_i^- = \sigma_{ij}n_j^- \tag{34}$$

results in

$$t_i^+ = \sigma_{ij}n_j^+ = -\sigma_{ij}n_j^- = -t_i. \tag{35}$$

For the intact bulk material the stress tensor σ in Eq. (7) is assumed to be linearly related to the (infinitesimal) strain tensor ε:

$$\sigma_{ij} = C_{ijkl}\varepsilon_{kl}. \tag{36}$$

Multiplying Eq. (7) by a test function δu_j and integrating over the domain Ω yields

$$\int_\Omega \delta u_{i,j}\sigma_{ij}\,\mathrm{dV} + \int_{\Gamma_d^+} \delta u_i^+ t_i\,\mathrm{dA} - \int_{\Gamma_d^-} \delta u_i^- t_i\,\mathrm{dA} = \int_{\partial\Omega_h} \delta u_i h_i\,\mathrm{dA} \tag{37}$$

after integration by parts, use of Gauss' theorem and application of the boundary conditions, Eqs. (8)–(35). Since $\int_{\Gamma_d^+} \dots \mathrm{dA} = \int_{\Gamma_d^-} \dots \mathrm{dA} = \int_{\Gamma_d} \dots \mathrm{dA}$, Eq. (37) can be replaced by

$$\int_\Omega \delta u_{i,j}\sigma_{ij}\,\mathrm{dV} + \int_{\Gamma_d} \delta[\![u_i]\!]t_i\,\mathrm{dA} = \int_{\partial\Omega_h} \delta u_i h_i\,\mathrm{dA} \tag{38}$$

with $[\![u_i]\!] = u_i^+ - u_i^-$ the crack opening.

4.2. Discretisation

Discretisation of the domain Ω into E elements,

$$\Omega = \bigcup_{e=1}^{E} \Omega^e, \tag{39}$$

and approximation of the displacements and their derivatives,

$$\underline{\boldsymbol{u}}^e = \underline{\underline{\mathbf{N}}}_u \underline{\boldsymbol{u}}, \qquad \delta\underline{\boldsymbol{u}}^e = \underline{\underline{\mathbf{N}}}_u \delta\underline{\boldsymbol{u}}, \qquad \underline{\boldsymbol{\varepsilon}}^e = \underline{\underline{\mathbf{B}}}_u \underline{\boldsymbol{u}}, \qquad \delta\underline{\boldsymbol{\varepsilon}}^e = \underline{\underline{\mathbf{B}}}_u \delta\underline{\boldsymbol{u}}, \tag{40}$$

with

$$\underline{\boldsymbol{u}}^e = \begin{bmatrix} u_1^e \\ u_2^e \end{bmatrix}, \qquad \delta\underline{\boldsymbol{u}}^e = \begin{bmatrix} \delta u_1^e \\ \delta u_2^e \end{bmatrix}, \qquad \underline{\boldsymbol{\varepsilon}}^e = \begin{bmatrix} \varepsilon_{11}^e \\ \varepsilon_{22}^e \\ 2\varepsilon_{12}^e \end{bmatrix}, \qquad \delta\underline{\boldsymbol{\varepsilon}}^e = \begin{bmatrix} \delta\varepsilon_{11}^e \\ \delta\varepsilon_{22}^e \\ 2\delta\varepsilon_{12}^e \end{bmatrix},$$

$$\underline{\underline{\mathbf{N}}}_u = \begin{bmatrix} N_1 & 0 & N_2 & 0 & \cdots \\ 0 & N_1 & 0 & N_2 & \cdots \end{bmatrix}, \qquad \underline{\underline{\mathbf{B}}}_u = \begin{bmatrix} N_{1,1} & 0 & N_{2,1} & 0 & \cdots \\ 0 & N_{1,2} & 0 & N_{2,2} & \cdots \\ N_{1,2} & N_{1,1} & N_{2,2} & N_{2,1} & \cdots \end{bmatrix} \tag{41}$$

results in the following matrix–vector equation:

$$\delta\underline{\boldsymbol{u}}^T \underbrace{\left(\int_\Omega \underline{\underline{\mathbf{B}}}_u^T \underline{\underline{\mathbf{C}}} \, \underline{\underline{\mathbf{B}}}_u \, \mathrm{dV} \underline{\boldsymbol{u}} + \int_{\Gamma_d} (\underline{\underline{\mathbf{N}}}_u^{+T} - \underline{\underline{\mathbf{N}}}_u^{-T})\underline{\boldsymbol{t}} \, \mathrm{dA} \right)}_{\underline{\boldsymbol{f}}_u^{\mathrm{int}}(\underline{\boldsymbol{u}})} - \delta\underline{\boldsymbol{u}}^T \underbrace{\int_{\partial\Omega_h} \underline{\underline{\mathbf{N}}}_u^T \underline{\boldsymbol{h}} \, \mathrm{dA}}_{\underline{\boldsymbol{f}}_u^{\mathrm{ext}}} = 0. \tag{42}$$

The traction $\underline{\boldsymbol{t}}$ in the global coordinate system can be obtained from the local traction $\underline{\boldsymbol{t}}_d$ via the transformation

$$\underline{\boldsymbol{t}} = \underline{\underline{\mathbf{Q}}}^T \underline{\boldsymbol{t}}_d, \tag{43}$$

with $\underline{\underline{\mathbf{Q}}}$ the orthogonal rotation matrix,

$$\underline{\underline{\mathbf{Q}}} = \underline{\underline{\mathbf{Q}}}^- = \begin{bmatrix} n_x^- & n_y^- \\ -n_y^- & n_x^- \end{bmatrix}, \tag{44}$$

and $\underline{\boldsymbol{n}}^-$ the normal vector from the minus side of the internal discontinuity, Γ_d^-, Fig. 16(b). $\underline{\boldsymbol{t}}_d$ is a function of the crack opening $[\![\underline{\boldsymbol{u}}_d]\!]$ in the local coordinate system of the discontinuity Γ_d, $\underline{\boldsymbol{t}}_d = \underline{\boldsymbol{t}}_d([\![\underline{\boldsymbol{u}}_d]\!])$. The local jump $[\![\underline{\boldsymbol{u}}_d]\!]$ can be evaluated from

$$[\![\underline{\boldsymbol{u}}_d]\!] = \underline{\underline{\mathbf{Q}}}[\![\underline{\boldsymbol{u}}]\!]. \tag{45}$$

The vectors for the local traction $\underline{\boldsymbol{t}}_d$ and local jump $[\![\underline{\boldsymbol{u}}_d]\!]$ consist of a normal and shear component

$$\underline{\boldsymbol{t}}_d = \begin{bmatrix} t_n \\ t_s \end{bmatrix}, \qquad [\![\underline{\boldsymbol{u}}_d]\!] = \begin{bmatrix} [\![u_n]\!] \\ [\![u_s]\!] \end{bmatrix}. \tag{46}$$

It is emphasised that the Bézier ordinates of the Bézier extraction operator in Eq. (5) that are required to compute $\underline{\underline{\mathbf{N}}}_u^+$ and $\underline{\underline{\mathbf{N}}}_u^-$ in Eq. (42) are different on both sides of the internal discontinuity Γ_d. This stems from the fact that pairs of Powell–Sabin triangles on either side of Γ_d are in general not symmetric, Fig. 17.

Since Eq. (42) must hold for any $\delta\underline{\boldsymbol{u}}$, the following discrete system results with $\underline{\boldsymbol{h}} = \underline{\boldsymbol{0}}$:

$$\underline{\boldsymbol{H}}(\underline{\boldsymbol{u}}, \lambda) = \begin{bmatrix} \underline{\boldsymbol{f}}_u^{\mathrm{int}}(\underline{\boldsymbol{u}}) - \lambda\hat{\underline{\boldsymbol{f}}} \\ \psi(\underline{\boldsymbol{u}}, \lambda) \end{bmatrix} = \underline{\boldsymbol{0}}, \tag{47}$$

where, again, λ is the loading parameter, $\hat{\underline{\boldsymbol{f}}}$ the normalised load vector and ψ an arc-length function. Linearisation of Eq. (47) yields the solution for the $i+1$th iteration in the $n+1$th increment:

$$\begin{bmatrix} \underline{\boldsymbol{u}} \\ \lambda \end{bmatrix}_{i+1}^{n+1} = \begin{bmatrix} \underline{\boldsymbol{u}} \\ \lambda \end{bmatrix}_i^{n+1} - \underline{\underline{\mathbf{K}}}_T^{-1} \Big|_i^{n+1} \cdot \begin{bmatrix} \underline{\boldsymbol{f}}_u^{\mathrm{int}}(\underline{\boldsymbol{u}}) - \lambda\hat{\underline{\boldsymbol{f}}} \\ \psi(\underline{\boldsymbol{u}}, \lambda) \end{bmatrix}_i^{n+1}, \tag{48}$$
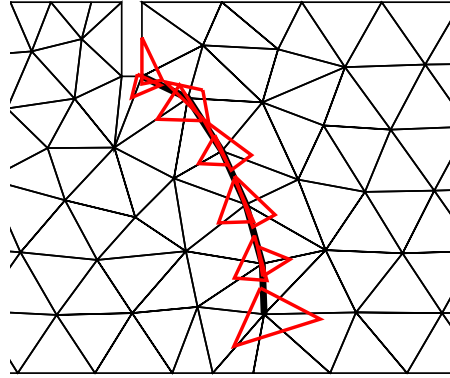
Fig. 17. Pairs of Powell–Sabin triangles (red) along the discontinuity Γ_d (thick black line) are not symmetric. This results in different Bézier ordinates for the Bézier extraction operator and in different basis functions $\underline{\underline{\mathbf{N}}}_u^+$ and $\underline{\underline{\mathbf{N}}}_u^-$ on both sides. (For interpretation of the references to colour in this figure legend, the reader is referred to the web version of this article.)

with

$$
\underline{\underline{\mathbf{K}}}_T(\underline{\boldsymbol{u}}, \lambda) =
\begin{bmatrix}
\dfrac{\partial \underline{\boldsymbol{f}}_u^{\text{int}}(\underline{\boldsymbol{u}})}{\partial \underline{\boldsymbol{u}}} & -\hat{\underline{\boldsymbol{f}}} \\[2mm]
\dfrac{\partial \psi(\underline{\boldsymbol{u}})}{\partial \underline{\boldsymbol{u}}} & \dfrac{\partial \psi(\underline{\boldsymbol{u}}, \lambda)}{\partial \lambda}
\end{bmatrix}
\tag{49}
$$

the tangential stiffness matrix.

Different from Section 3, a dissipation-based arc-length method for ψ is not used. Since the crack length does not increase in each increment, new interfaces are not inserted in each increment. Therefore, the amount of energy that can be dissipated is different depending on whether a new cohesive element has been added or not, which makes the use of an energy-based constraint less obvious. Instead, an arc-length method has been employed which controls the crack mouth sliding displacement (CMSD) [34], although the present formulation is slightly different. Herein, the constraint

$$
u_n^{\text{R}} - u_n^{\text{L}} = n \Delta \bar{u}_{\text{CMSD}}
\tag{50}
$$

is enforced, where u_n^{R} is the displacement on the right and u_n^{L} is the displacement on the left tip of the notch (Fig. 11) in the nth increment, and $\Delta \bar{u}_{\text{CMSD}}$ the prescribed CMSD. In the $n+1$th increment,

$$
u_{n+1}^{\text{R}} - u_{n+1}^{\text{L}} = (n+1) \Delta \bar{u}_{\text{CMSD}}
\tag{51}
$$

must be fulfilled. Subtracting Eq. (50) from Eq. (51) results in

$$
u_{n+1}^{\text{R}} - u_n^{\text{R}} - (u_{n+1}^{\text{L}} - u_n^{\text{L}}) = (n+1-n) \Delta \bar{u}_{\text{CMSD}},
\tag{52}
$$

$$
\Delta u^{\text{R}} - \Delta u^{\text{L}} = \Delta \bar{u}_{\text{CMSD}},
\tag{53}
$$

so that the following arc-length method constraint applies in each increment

$$
\psi(\underline{\boldsymbol{u}}) = \Delta u^{\text{R}} - \Delta u^{\text{L}} - \Delta \bar{u}_{\text{CMSD}}.
\tag{54}
$$

Since ψ depends only on the displacement vector $\underline{\boldsymbol{u}}$ in Eq. (54), the term $\frac{\partial \psi(\underline{\boldsymbol{u}}, \lambda)}{\partial \lambda}$ becomes zero in Eq. (49). This would result in a singular tangential stiffness matrix $\underline{\underline{\mathbf{K}}}_T$. Therefore, Eq. (48) cannot be used to solve our problem. However,
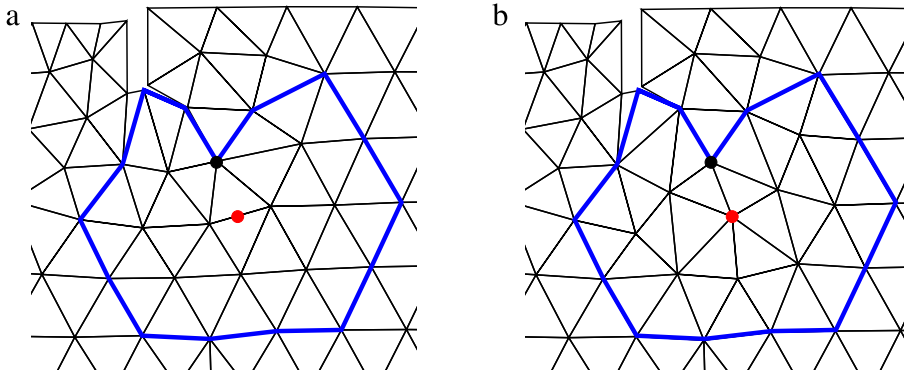
Fig. 18. Mesh in the deformed configuration (a) before and (b) after re-meshing. The black circle marks the old crack tip where the critical stress t_{ult} is exceeded. The red circle shows the location of the new crack tip. Within the blue polygon, a local re-meshing procedure is applied. Vertices along the existing crack path, the new crack tip and vertices on and outside the blue polygon are held fixed. (For interpretation of the references to colour in this figure legend, the reader is referred to the web version of this article.)

the linearised form of Eq. (47) can be solved for $\underline{u}_{i+1}^{n+1}$ and λ_{i+1}^{n+1} in a staggered manner [35]. At first, we solve for

$$\delta \underline{u}_{i+1}^{n+1\,I} = \left(\frac{\partial \underline{f}_{-u}^{\text{int}}(\underline{u})}{\partial \underline{u}} \bigg|_{i}^{n+1} \right)^{-1} \cdot \hat{\underline{f}}, \tag{55}$$

$$\delta \underline{u}_{i+1}^{n+1\,II} = \left(\frac{\partial \underline{f}_{-u}^{\text{int}}(\underline{u})}{\partial \underline{u}} \bigg|_{i}^{n+1} \right)^{-1} \cdot \left(\lambda_{i}^{n+1} \hat{\underline{f}} - \underline{f}_{-u}^{\text{int}}(\underline{u}_{i}^{n+1}) \right) \tag{56}$$

and use these to compute

$$\delta \lambda_{i+1}^{n+1} = \frac{-\psi - \frac{\partial \psi}{\partial \underline{u}} \delta \underline{u}_{i+1}^{n+1\,II}}{\frac{\partial \psi}{\partial \underline{u}} \delta \underline{u}_{i+1}^{n+1\,I} + \frac{\partial \psi}{\partial \lambda}}, \tag{57}$$

$$\delta \underline{u}_{i+1}^{n+1} = \delta \lambda_{i+1}^{n+1} \delta \underline{u}_{i+1}^{n+1\,I} + \delta \underline{u}_{i+1}^{n+1\,II}. \tag{58}$$

Finally, we obtain

$$\underline{u}_{i+1}^{n+1} = \underline{u}_{i}^{n+1} + \delta \underline{u}_{i+1}^{n+1}, \tag{59}$$

$$\lambda_{i+1}^{n+1} = \lambda_{i}^{n+1} + \delta \lambda_{i+1}^{n+1}. \tag{60}$$

4.3. Re-meshing

After obtaining an equilibrium in increment $n+1$ for Eq. (47), the first principal stress at the crack tip (black vertex in Fig. 18) is evaluated. Benefiting from the $\mathcal{C}^1$-continuity, it can be directly computed at the vertex. When the first principal stress exceeds the critical stress t_{ult}, the vector normal to the first principal stress direction is computed. The location, where this vector intersects an element edge is highlighted red in Fig. 18. This marks the location of the new crack tip. As a next step, elements in the neighbourhood of the new crack tip have to be re-meshed while the position of the vertices along the crack path and the new crack tip are held fixed. For instance, vertices on and outside the blue polygon and the new crack tip in Fig. 18 are not allowed to move and re-meshing is applied within the blue polygon. For local re-meshing, the approach from [36] is used which interprets the mesh as a truss structure and finds an equilibrium such that forces at the vertices are zero.

After re-meshing, we have to determine locally the new Powell–Sabin triangles and solve again Eq. (47) for increment $n+1$ with the extended crack. When solving Eq. (47) for increment $n+1$, the displacement vector $\tilde{\underline{u}}_{n}$
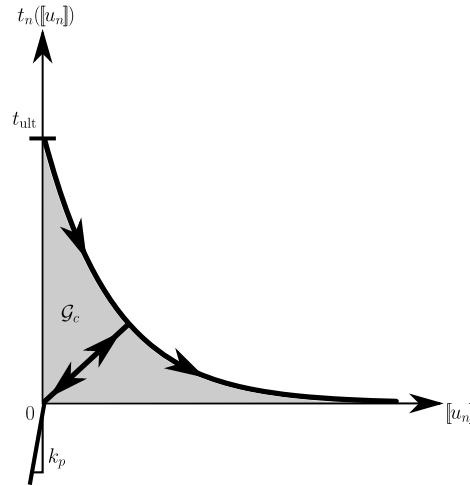
Fig. 19. Cohesive traction law in the normal direction. The branch represents unloading for the case $[\![u_n]\!] < \kappa$. The shaded grey area is equivalent to the fracture energy $\mathcal{G}_c$.

for increment n on the updated mesh is required. In order to find the displacement vector $\tilde{\underline{\boldsymbol{u}}}_n$, the following problem is solved locally for the re-meshed domain

$$\min \left(\frac{1}{2} \int_\Omega \| \underline{\tilde{\mathbf{N}}}_u \tilde{\boldsymbol{u}}_n - \underline{\mathbf{N}}_u \boldsymbol{u}_n \|_2^2 \, \mathrm{dV} \right), \tag{61}$$

where $\underline{\tilde{\mathbf{N}}}_u$ contains the basis functions on the updated mesh. Eq. (61) results in the system

$$\int_\Omega \underline{\tilde{\mathbf{N}}}_u^T \underline{\tilde{\mathbf{N}}}_u \tilde{\boldsymbol{u}}_n \, \mathrm{dV} = \int_\Omega \underline{\tilde{\mathbf{N}}}_u \underline{\mathbf{N}}_u \boldsymbol{u}_n \, \mathrm{dV}, \tag{62}$$

which can be solved directly for $\tilde{\underline{\boldsymbol{u}}}_n$.

4.4. Single-edge notched beam

As an example, the Single-Edge Notched Beam is re-considered. The parameters and coefficients have been taken from [10]. The material parameters are: Young's modulus $E = 35{,}000$ MPa and Poisson's ratio $\nu = 0.2$ with a plane-stress assumption. The concrete is modelled linearly elastic. The thickness of the beam is $t = 100$ mm and the value of the critical stress is set to $t_{\mathrm{ult}} = 2.8$ MPa. For the local traction $\boldsymbol{t}_d$, the relations from [5] are used. The cohesive law in the normal direction reads

$$t_n = t_{\mathrm{ult}} \exp\left(-\frac{t_{\mathrm{ult}}}{\mathcal{G}_c} \kappa \right), \tag{63}$$

see Fig. 19, where the history parameter κ is determined by the loading function $f = [\![u_n]\!] - \kappa$ which evolves according to the Karush–Kuhn–Tucker conditions of Eq. (11). The fracture energy and the penetration stiffness are taken as $\mathcal{G}_c = 0.1$ N/mm and $k_p = 10^4$ N/mm^3, respectively.

In the shear direction,

$$t_s = d_{\mathrm{int}} [\![u_s]\!] \tag{64}$$

has been used with an initial shear stiffness $d_{\mathrm{int}} = 1$ MPa/mm. At the onset of the simulation, $\Delta \bar{u}_{\mathrm{CMSD}} = 1.5 \times 10^{-3}$ mm has been taken. Fig. 20 shows the resulting force–displacement curves for six different mesh sizes. The mesh is refined uniformly. Along the x-axis, the CMSD is plotted, while the y-axis gives the reaction force $P = \frac{11}{10}\lambda$. The legend entry displays the number of degrees of freedom at the beginning and at the end of the simulation. Fig. 21 shows the final crack paths for six different discretisations. Fig. 22 gives the stress field σ_{xx} at CMSD $= 0.04$ mm for the mesh with 49632–49860 degrees of freedom. This mesh size is equivalent to that using the implicit fourth-order
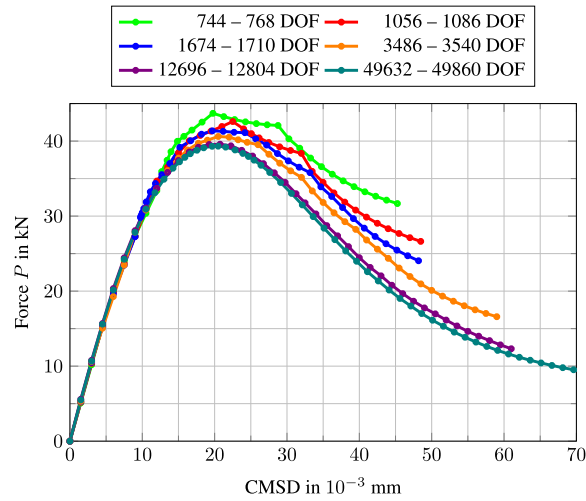
Fig. 20. Force–displacement curve for the SENB with cohesive zone modelling for six different mesh sizes.
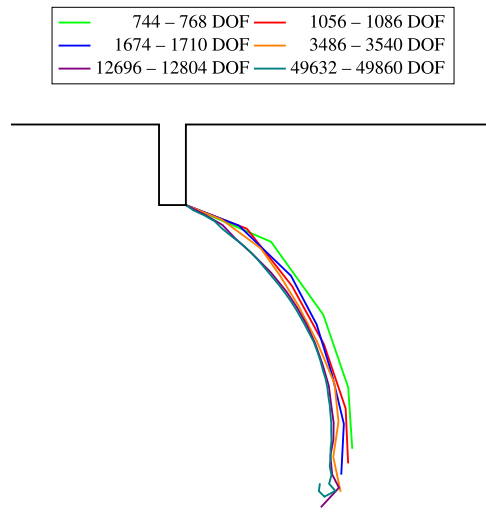

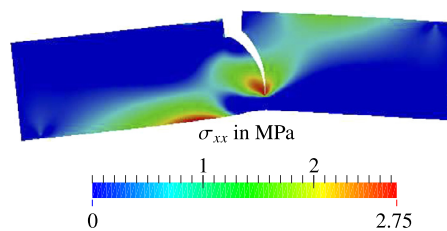Fig. 21. Final crack paths for six different mesh sizes.

Fig. 22. Stress field σ_{xx} for the SENB in the deformed configuration at a CMSD of 0.04 mm for the mesh with 49632–49860 degrees of freedom. Displacements are amplified by a factor of 200. The mesh size is equivalent to the one showing the results for the implicit fourth-order gradient damage model in Fig. 15.

gradient damage model with 74,448 degrees of freedom, Fig. 15. Finally, Fig. 23 gives an overlap of the initial and final mesh with 744 and 768 degrees of freedom, respectively.
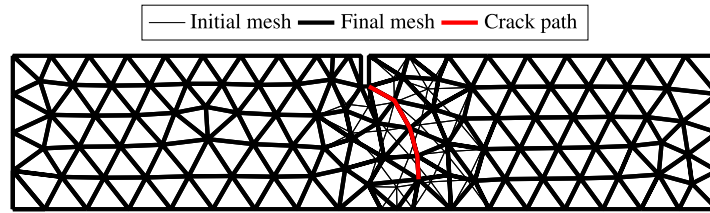
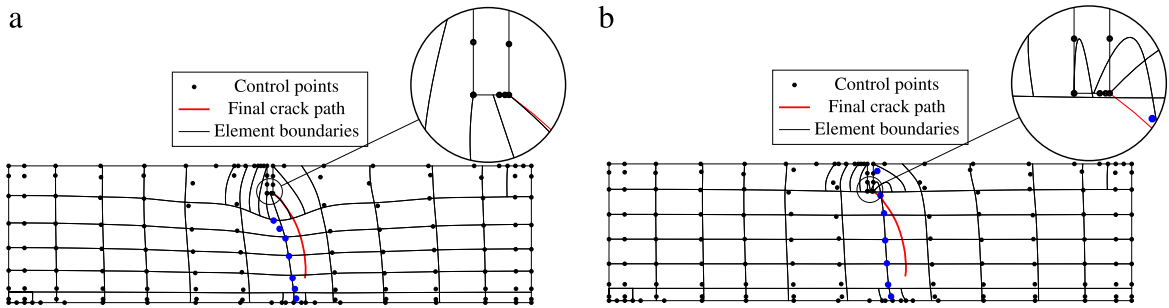Fig. 23. Comparison of the initial (744 degrees of freedom) and the final mesh (768 degrees of freedom).

Fig. 24. Cohesive zone modelling using structured T-splines. (a) T-spline mesh from [10] when the location of the blue control points is prescribed. (b) Not prescribing the location of the blue control points results in inverted elements around the notch. (For interpretation of the references to colour in this figure legend, the reader is referred to the web version of this article.)

The discrete approach with cohesive zones along the crack path requires less degrees of freedom than the implicit fourth order gradient damage model for numerical results that are in good agreement with the experiments carried out in [33]. Also, since derivatives of second order are required for the implicit fourth order gradient damage model, the computation of the tangential stiffness matrix and force vector is more expensive. Nevertheless, implementation is easier for the implicit fourth order gradient damage model since no re-meshing is necessary.

4.5. The use of structured T-splines for the single-edge notched beam

Structured T-splines have been used for cohesive zone modelling for the Single-Edge Notched Beam in [10]. Fig. 24(a) shows the initial T-spline mesh. In order to determine the position of the control points, an elliptic problem is solved in the parameter domain, while the location of some control points has to be prescribed, for instance control points on the boundary. It is observed from Fig. 24 that not only the position of control points on the boundary, but also the position of the blue control points in the interior has to be prescribed. Furthermore, the blue control points have to be positioned such that the initial mesh has to be aligned with the final crack path (red). Only then, elements can be split vertically. If the location of the blue control points were not prescribed, the mesh in Fig. 24(b) would be obtained after solving the elliptic problem in the parameter domain. This would result in inverted elements around the notch. Since the final crack path is not always known a priori, the capabilities of structured T-splines to model discrete fracture therefore seem somewhat limited. Furthermore, the degree of continuity across elements sharing one edge that touches the crack tip is only $\mathcal{C}^0$, so that stresses need to be evaluated and weighted at the integration points in the vicinity of the crack tip in order to determine when the critical stress t_{ult} is reached, which detracts from the usual gain in terms of accuracy of splines compared to Lagrangian basis functions.

5. Concluding remarks

Powell–Sabin B-splines can be an appealing alternative to NURBS or T-splines when applied to damage and fracture. $\mathcal{C}^1$-continuous Powell–Sabin B-splines can be obtained from any triangulation and Bézier extraction allows an efficient computation. The $\mathcal{C}^1$-continuity of Powell–Sabin B-splines makes them suitable candidates not only for the implicit fourth-order gradient damage model, but also for discrete fracture simulations, since they remain $\mathcal{C}^1$-continuous at the crack tip. This property allows for a direct evaluation of stresses at the crack tip. Furthermore,

re-meshing Powell–Sabin B-splines is always possible and the initial mesh does not have to be aligned with the final crack path as for structured T-splines.

A disadvantage of Powell–Sabin splines is that there is at present no procedure for obtaining Powell–Sabin B-splines on arbitrary tetrahedral meshes in three dimensions since certain constraints with neighbouring tetrahedrons have to be fulfilled [37]. Hence, three-dimensional Powell–Sabin B-splines currently work only for structured meshes. Indeed, a "perfect" solution for $\mathcal{C}^1$-continuous tetrahedra does not (yet) seem to exist [38].

Acknowledgement

References

[1] A.R. Ingraffea, V. Saouma, Numerical modelling of discrete crack propagation in reinforced and plain concrete, in: Fracture Mechanics of Concrete, Martinus Nijhoff Publishers, Dordrecht, 1985, pp. 171–225.

[2] G.T. Camacho, M. Ortiz, Computational modelling of impact damage in brittle materials, Int. J. Solids Struct. 33 (1996) 2899–2938.

[3] T. Belytschko, T. Black, Elastic crack growth in finite elements with minimal remeshing, Internat. J. Numer. Methods Engrg. 45 (1999) 601–620.

[4] N. Moës, J. Dolbow, T. Belytschko, A finite element method for crack growth without remeshing, Internat. J. Numer. Methods Engrg. 46 (1999) 131–150.

[5] G.N. Wells, L.J. Sluys, A new method for modelling cohesive cracks using finite elements, Internat. J. Numer. Methods Engrg. 50 (2001) 2667–2682.

[6] G.N. Wells, L.J. Sluys, A consistent geometrically non-linear approach for delamination, Internat. J. Numer. Methods Engrg. 54 (2002) 1333–1355.

[7] J.J.C. Remmers, R. de Borst, A. Needleman, A cohesive segments method for the simulation of crack growth, Comput. Mech. 31 (2003) 69–77.

[8] J. Réthoré, R. de Borst, M.A. Abellan, A two-scale approach for fluid flow in fractured porous media, Internat. J. Numer. Methods Engrg. 75 (2007) 780–800.

[9] J. Réthoré, R. de Borst, M.A. Abellan, A two-scale model for fluid flow in an unsaturated porous medium with cohesive cracks, Comput. Mech. 42 (2008) 227–238.

[10] C.V. Verhoosel, M.A. Scott, R. de Borst, T.J.R. Hughes, An isogeometric approach to cohesive zone modeling, Internat. J. Numer. Methods Engrg. 87 (2011) 336–360.

[11] P. Kagan, A. Fischer, P.Z. Bar-Yoseph, New B-spline finite element approach for geometrical design and mechanical analysis, Internat. J. Numer. Methods Engrg. 41 (1998) 435–458.

[12] T.J.R. Hughes, J.A. Cottrell, Y. Bazilevs, Isogeometric analysis: CAD, finite elements, NURBS, exact geometry and mesh refinement, Comput. Methods Appl. Mech. Engrg. 194 (2005) 4135–4195.

[13] M.J.D. Powell, M.A. Sabin, Piecewise quadratic approximations on triangles, ACM Trans. Math. Software 3 (1977) 316–325.

[14] H. Speleers, P. Dierckx, S. Vandewalle, Numerical solution of partial differential equations with Powell–Sabin splines, J. Comput. Appl. Math. 189 (2006) 643–659.

[15] R. de Borst, J.J.C. Remmers, A. Needleman, M.A. Abellan, Smeared crack vs discrete crack models for concrete fracture: bridging the gap, Int. J. Numer. Anal. Methods Geomech. 28 (2004) 583–607.

[16] G. Pijaudier-Cabot, Z.P. Bažant, Nonlocal damage theory, J. Eng. Mech. 113 (1987) 1512–1533.

[17] R.H.J. Peerlings, R. de Borst, W.A.M. Brekelmans, J.H.P. de Vree, Gradient enhanced damage for quasi-brittle materials, Internat. J. Numer. Methods Engrg. 39 (1996) 3391–3403.

[18] R.H.J. Peerlings, M.G.D. Geers, R. de Borst, W.A.M. Brekelmans, A critical comparison of nonlocal and gradient-enhanced softening continua, Int. J. Solids Struct. 38 (2001) 7723–7746.

[19] C.V. Verhoosel, M.A. Scott, T.J.R. Hughes, R. de Borst, An isogeometric analysis approach to gradient damage models, Internat. J. Numer. Methods Engrg. 86 (2011) 115–134.

[20] P. Dierckx, On calculating normalized Powell–Sabin B-splines, Comput. Aided Geom. Design 15 (1997) 61–78.

[21] S. May, J. Vignollet, R. de Borst, Powell–Sabin B-splines and unstructured T-splines for the solution of Kirchhoff–Love plate theory exploiting Bézier extraction, Int. J. Numer. Methods Eng. (2016) http://dx.doi.org/10.1002/nme.5163.

[22] H. Speleers, C. Manni, F. Pelosi, M.L. Sampoli, Isogeometric analysis with Powell–Sabin splines for advection-diffusion-reaction problems, Comput. Methods Appl. Mech. Engrg. 221–222 (2012) 132–148.

[23] E. Vanraes, P. Dierckx, A. Bultheel, On the Choice of the PS-triangles, Tech. Rep. 353, KU Leuven, Department of Computer Science, K.U. Leuven, 2003.

[24] W. Karush, Minima of functions of several variables with inequalities as side constraints (Master's thesis), University of Chicago, 1939.

[25] H.W. Kuhn, A.W. Tucker, Nonlinear programming, in: Second Berkeley Symposium on Mathematical Statistics and Probability, 1951, pp. 481–492.

[26] S. May, J. Vignollet, R. de Borst, A new arc-length control method based on the rates of the internal and the dissipated energy, Eng. Comput. 33 (2016) 100–115.

[27] S. Lipton, J.A. Evans, Y. Bazilevs, T. Elguedj, T.J.R. Hughes, Robustness of isogeometric structural discretizations under severe mesh distortion, Comput. Methods Appl. Mech. Engrg. 199 (2010) 357–373.

[28] S. May, J. Vignollet, R. de Borst, The role of the Bézier extraction operator for T-splines of arbitrary degree: linear dependencies, partition of unity property, nesting behaviour, and local refinement, Internat. J. Numer. Methods Engrg. 103 (2015) 247–281.

[29] C.A. Felippa, Introduction to finite element methods, in: Course Notes, Department of Aerospace Engineeing Sciences, University of Colorado at Boulder, 2004.

[30] J.H.P. De Vree, W.A.M. Brekelmans, M.A.J. Van Gils, Comparison of nonlocal approaches in continuum damage mechanics, Comput. Struct. 55 (4) (1995) 581–588.

[31] M.G.D. Geers, R. De Borst, W.A.M. Brekelmans, R.H.J. Peerlings, Strain-based transient-gradient damage model for failure analyses, Comput. Methods Appl. Mech. Engrg. 160 (1998) 133–153.

[32] M.A. Gutiérrez, Energy release control for numerical simulations of failure in quasi-brittle solids, Commun. Numer. Methods. Eng. 20 (2004) 19–29.

[33] E. Schlangen, Experimental and numerical analysis of fracture processes in concrete (Ph.D. thesis), Delft University of Technology, 1993.

[34] R. de Borst, Computation of post-bifurcation and post-failure behavior of strain-softening solids, Comput. Struct. 25 (1987) 211–224.

[35] R. de Borst, M.A. Crisfield, J.J.C. Remmers, C.V. Verhoosel, Nonlinear Finite Element Analysis of Solids and Structures, John Wiley & Sons, 2012.

[36] P.-O. Persson, G. Strang, A simple mesh generator in MATLAB, SIAM Rev. 46 (2004) 329–345.

[37] A.J. Worsey, B. Piper, A trivariate Powell–Sabin interpolant, Comput. Aided Geom. Design 5 (1988) 177–186.

[38] P. Alfeld, T. Sorokina, Two tetrahedral C^1 cubic macro elements, J. Approx. Theory 157 (2009) 53–69.